

Analytical model for extracting intrinsic fluorescence in turbid media

Jun Wu, Michael S. Feld, and Richard P. Rava

In this paper we describe a photon migration approach for modeling fluorescence in an optically thick, turbid medium such as human tissue. In such a medium the intrinsic fluorescence spectrum of the fluorophores ϕ can be distorted by the interplay of many factors, including scattering and absorption, excitation and collection geometries, and boundary conditions. The model provides an analytical relationship between the bulk fluorescence spectrum F and the diffuse reflectance spectrum R for arbitrary geometries and boundary conditions. We demonstrate that the distortion can be simply and accurately removed by measuring R from the optically thick medium over the same wavelength range and in the same manner as F . Over a wide range of tissue parameters this relationship may be written as $\phi \propto F/R_{\text{eff}}$, with R_{eff} a corrected form of the measured diffuse reflectance. The validity of this approach is demonstrated in both laboratory experiments on human aortic media and by comparison with Monte Carlo simulations and diffusion theory. Connection with a previous algorithm for extracting intrinsic fluorescence is also discussed.

Key words: Fluorescence, diffuse reflectance.

1. Introduction

Fluorescence spectroscopy has been widely explored as an important medical diagnostic technique. Promising results have been reported when tissue autofluorescence is used to detect a diversity of diseases, such as atherosclerosis in the aorta and the coronary artery¹⁻³ and dysplasia in the colon and other tissues.⁴ A majority of the diagnostic methods employed utilize empirical algorithms derived from studying a limited number of specimens. Such empirical algorithms ignore the wealth of biochemical and/or morphological information contained in the tissue spectrum. Part of the difficulty has been that fluorescence spectra observed from optically thick tissue is distorted from the intrinsic spectra of individual fluorescence chromophores by the interplay of factors such as scattering, absorption, geometry, and tissue boundary conditions. Thus experiments utilizing optical-fiber probes in the clinical setting often yield results that are different from those utilizing a laboratory spectrofluorimeter. In addition the experimental data also depend on whether the tissue-

environment boundary condition is index matched or index mismatched.

A model that can remove the distorting effects on the fluorescence spectra of optically thick tissues would allow connection of the clinically obtained *in vivo* tissue spectra with their biochemically based fluorophores. Algorithms that incorporate the effects of the intrinsic fluorescence, scattering, absorption, excitation and collection geometries, and the tissue boundary conditions, must be developed for us to move beyond the current empirical approaches. Such algorithms will allow the accurate extraction of the information of the physiochemical composition of the tissue and thus provide biochemical and morphological information about tissue pathology for tracking the development of disease *in vivo*.

Recently photon migration models have been examined for their ability to explain the diffuse reflectance spectra in tissue.⁵ Simple analytical expressions have been derived that describe the observed reflectance spectra over a range of scattering and absorption coefficients typically found in human tissue.⁶ The purpose of the present study is to extend the photon migration picture to model the fluorescence from turbid media such as human tissue. The algorithm determined from the photon migration approach suggests that the distortion in a fluorescence spectrum caused by the interplay of scattering, absorption, geometry, and boundary conditions can be pre-

The authors are with the George R. Harrison Spectroscopy Laboratory, Massachusetts Institute of Technology, Cambridge, Massachusetts 02139.

Received 2 June 1992.

0003-6935/93/193585-11\$06.00/0.

© 1993 Optical Society of America.

cisely removed by measuring the diffuse reflectance spectrum over the same wavelength range, and in the same manner as the fluorescence spectrum, and by applying this diffuse reflectance spectrum to the fluorescence spectrum in a well-defined manner. The result is the same intrinsic fluorescence spectrum as would be obtained from thin (10- μm) tissue slices that are not distorted by these factors.

In Section 2 we review the theoretical approaches used throughout this paper. A diffusion theory model for fluorescence is examined first, followed by a Monte Carlo simulation that is used for comparison below. The photon migration model for a one-layer homogeneous tissue fluorescence is then derived. The results of the analytical expressions from diffusion theory and the photon migration model are compared with simulations and experiments in Section 3 and discussed in Section 4.

2. Theoretical Approaches

A. Theoretical Methods

1. Diffusion Theory Calculation for Fluorescence

As shown in Appendix A, from diffusion theory one can determine an expression for the observed bulk tissue fluorescence intensity $F(\lambda_x, \lambda_m)$ from a semi-infinite slab:

$$F(\lambda_x, \lambda_m) = \mu_a(\lambda_x)\phi(\lambda_x, \lambda_m) \times \left[\frac{4\pi A(\lambda_x) + F_0}{\mu_t(\lambda_x) + \kappa_d(\lambda_m)} + \frac{4\pi C_2(\lambda_x)}{\kappa_d(\lambda_x) + \kappa_d(\lambda_m)} \right] C(\lambda_m), \quad (1)$$

where λ_x and λ_m are the excitation and emission wavelengths, respectively, and the other quantities are fully described in Appendix A. Although Eq. (1) could be used to fit an experimentally obtained spectrum, it does not provide a practical method for extracting the quantum yield or intrinsic fluorescence $\phi(\lambda_x, \lambda_m)$ from the optically thick tissue spectrum. As is seen below, the photon migration picture provides such an expression directly.

2. Monte Carlo Methods

The Monte Carlo method performs by recording individual photon-tissue interactions in a straightforward manner. A photon injected into tissue is allowed to travel freely for approximately one mean free path, based on the tissue parameters, before it interacts with a tissue particle. On interaction the photon is either scattered, absorbed, or reemitted as fluorescence. If scattered or reemitted, it travels in a new direction determined by the phase function for scattering or fluorescence. For a semi-infinite slab tissue the process is allowed to continue until the photon is either absorbed or reemitted out of the tissue.

To simulate the actual physical process, the Monte Carlo method uses a random number generator to sample random variables, such as the path length between two interaction events and the occurrence of

absorption, fluorescence, and the scattering angle. The values of these variables are chosen randomly from their probability distributions. In our simulations the following probability distribution functions and procedures are utilized:

(1) The probability of a photon traveling a path length L is determined by the sum of the absorption and scattering coefficients, $\mu_t = \mu_s + \mu_a$. When Beer's law is used, the probability distribution function of the path length $p(L)$ is given by $p(L) = \mu_t \exp(-\mu_t L)$.

(2) The probability of a photon being absorbed on interaction with a tissue particle, $p(\text{absorption})$, depends on both the absorption and the scattering coefficients and is given by $p(\text{absorption}) = \mu_a / (\mu_s + \mu_a)$. At each interaction the photon weight⁷ decreases by the factor $1 - p(\text{absorption})$.

(3) On absorption the probability of generating a fluorescence photon from an excitation wavelength λ_x and at an emission wavelength λ_m is given by the quantum yield $\phi(\lambda_x, \lambda_m)$. This represents the intrinsic tissue fluorescence, unaffected by scattering, absorption, geometry, or boundary conditions.

(4) Fluorescence events are handled separately from the scattering events, and fluorescence is emitted isotropically (i.e., the anisotropy coefficient for a fluorescence event $g = 0$).

(5) The deflection angle in a single scattering event is determined by the Henyey-Greenstein phase function, which provides a good representation of scattering in tissue.⁸

(6) The internal reflection versus transmission at the boundary is determined by Fresnel's reflection relationships and Snell's law.⁹

In the simulations the incident beam profile can be either uniform or Gaussian. The calculations presented in this paper utilize uniform beam profiles. In addition the beam can be either collimated or divergent. For simplicity a collimated beam is used in our calculations here. (An optical fiber with a numerical aperture of 0.22 has a half-angle of divergence of only 12.7°).

The Monte Carlo program utilized in this paper works in a manner similar to other reported models,⁷ except for three features: (1) Its ability to handle fluorescence. (2) Its photon launching technique. Photons are launched from the entire beam profile, so that no convolution calculations need to be carried out afterward. (3) Its photon termination technique. A photon is terminated naturally if it is reemitted from the tissue. In addition, if the photon weight falls below some prescribed minimum value, the outcomes of the subsequent interactions are randomly sampled, and the photon weight is either kept the same or set to zero (photon termination), depending on whether the interaction is sampled as a scattering event or an absorption event.

When a large number of photons are used, the Monte Carlo method allows a statistically precise

result to be obtained. Therefore it usually serves as a reliable standard for testing the accuracy of other models. Our program showed agreement with standard results.¹⁰

B. Fluorescence Photon Migration

1. Introduction

In a recent paper⁶ we described a photon migration approach to modeling the diffuse reflectance from a semi-infinite, index-matched turbid medium, such as human tissue. In our method the phase-function dependence of the scattering is separated from the scattering and absorption coefficients by introducing an escape probability distribution function $f_n(g)$, which describes the probability of a photon with the scattering anisotropy coefficient g escaping from the tissue sample after n scattering events. The parameter g is usually a weak function of wavelength¹¹; in the following it will be considered to be constant over the wavelength range of interest. In this model, which corresponds to the ensemble average point of view of the actual physical picture, every photon is eventually reemitted but with a reduced weight reflecting the number of interactions the photon has undergone before leaving the tissue. For a photon scattered n times before being reemitted, the weight of the photon is given by a^n , where the albedo $a = \mu_s/(\mu_a + \mu_s)$. The diffuse reflectance R is then given by

$$R(a, g) = \sum_{n=1}^{\infty} a^n f_n(g).$$

Using this approach, we derived two analytical expressions that could be used to calculate R as a function of the quantity $-\ln(a)/(1-g)$. Under the simplifying assumption that the $f_n(g)$ curve can be represented by an exponentially decreasing function of n , $f_n(g) = S(1-g)\exp[-S(1-g)n]$, we found

$$R(\mu_a, \mu_s, g) = \frac{1}{1 - \frac{1}{S} \frac{\ln(a)}{1-g}}, \quad (2)$$

where S is a constant approximately equal to $1/14$. Equation (2) agrees with both the Monte Carlo calculations and experimental data over a range $\mu_s(1-g)/\mu_a < 10$, which covers many human tissues. An expression for R with a broader range of validity was also derived.⁶

2. Monte Carlo Simulations of the Escape Probability Curves

Equation (2) is derived for a semi-infinite geometry in index-matched boundary conditions. To extend Eq. (2), we need to demonstrate that in a diverse set of collection geometries and boundary conditions, $f_n(g)$ behaves similarly and can still be approximated by an exponential function. This will sometimes be useful in the following discussions. Figure 1 shows $f_n(g)$ curves computed from Monte Carlo simulations for

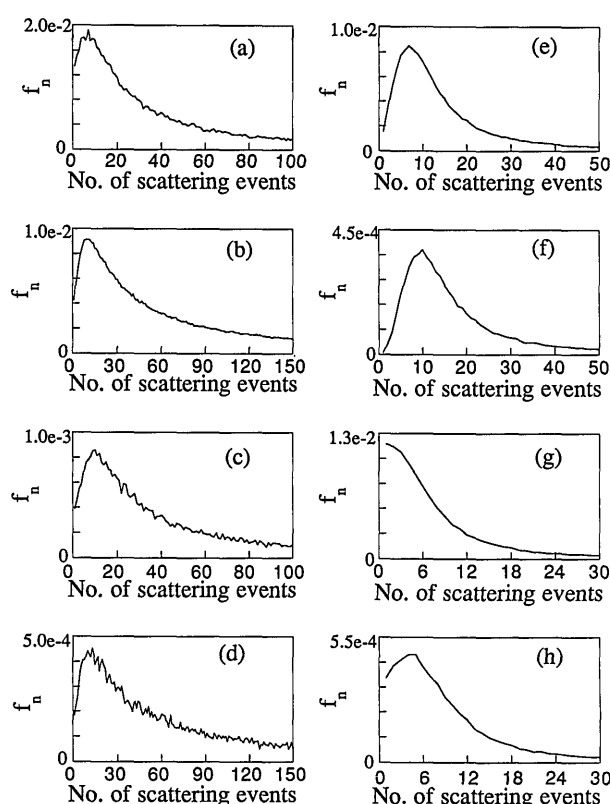


Fig. 1. Monte Carlo simulations of $f_n(g)$ for different collection geometries and boundary conditions. The collection geometries and boundary conditions are summarized in Table 1.

several different boundary conditions and geometries. A value of $g = 0.8$, typically of biological tissue, was assumed. The geometry and boundary condition for each $f_n(g = 0.8)$ curve studied are summarized in Table 1. All the $f_n(g)$ curves exhibit a similar line shape, rising to a peak value for a small number of scattering events and falling to zero for a large number of scattering events; however, the x and y scales in each of the curves in Fig. 1 are different. The index-mismatched boundary conditions [Figs.

Table 1. Summary of the Geometries and Boundary Conditions for Calculating the $f_n(g = 0.8)$ Curves Shown in Fig. 1

Figure	Light Delivery	Collection Area	Collection Angle (deg)	Relative Refractive Index
1(a)	Plane wave	Infinitely wide ^a	0-90	1.0
1(b)	Plane wave	Infinitely wide ^a	0-90	1.4
1(c)	Plane wave	Infinitely wide ^a	0-12.7	1.0
1(d)	Plane wave	Infinitely wide ^a	0-12.7	1.4
1(e)	Optical fiber ^b	$D/2 < r < D$	0-90	1.0
1(f)	Optical fiber ^b	$D/2 < r < D$	0-12.7	1.0
1(g)	Optical fiber ^b	$0 < r < D/2$	0-90	1.0
1(h)	Optical fiber ^b	$0 < r < D/2$	0-12.7	1.0

^aThe same result is expected independent of the light delivery profile when the light collection area is infinitely wide.

^bA uniform and collimated beam is assumed out of the optical fiber end with a diameter $D = 6/\mu_t$; this represents a typical *in vivo* experimental geometry utilizing a 200- μ m core fiber with a tissue attenuation coefficient of $\mu_t = 30 \text{ mm}^{-1}$.

1(b) and 1(d)] always tend to spread the f_n curve in the x direction and compress it in the y direction. On the other hand, the fiber probe geometry [Figs. 1(e)–1(h)] tends to compress the f_n curve in both the x and y scales. This suggests that an exponential function can still be used to approximate $f_n(g)$, except that the numerical constants in the exponential function now depend on the geometry and boundary conditions: $f_n(g) = k_0 S' (1 - g) \exp[-S' (1 - g)n]$. The effect on Eq. (2) is that

$$\frac{R}{k_0} = \frac{1}{1 - \frac{1}{S'} \ln(a)}, \quad (2')$$

where k_0 is a normalization constant (replacing 1). Both k_0 and S' are constants for a given geometry and refractive-index mismatch at the boundary. The parameter $R/k_0 = R^{\text{obs}}$ is the quantity usually measured in diffuse reflectance experiments, since the reflectance from tissue is almost always compared with that from some standard such as BaSO_4 . To demonstrate the wider validity of Eq. (2'), we chose two extreme cases, 1(f) and 1(h) of Table 1, to calculate the diffuse reflectance using the Monte Carlo method. Figure 2 shows that the diffuse reflectance data can be fit by Eq. (2') quite well.

3. Fluorescence Photon Migration

In the photon migration picture, on interaction with a tissue particle, an incident photon is always scattered with its weight reduced by a factor $a(\lambda_x)$, depositing $[1 - a(\lambda_x)]$ of its weight in the tissue. On absorption the photon has a certain probability of being reemitted at a fluorescence wavelength λ_m , which is given by the quantum yield $\phi(\lambda_x, \lambda_m)$. The weight of the fluorescent photon is then $[1 - a(\lambda_x)]\phi(\lambda_x, \lambda_m)$ times the original weight of the incident photon just before the interaction. The fluorescent photon is emitted isotropically and undergoes scattering on its way of the tissue, lowering its weight by $a(\lambda_m)$ at each scattering interaction. In our model we assume that the secondary fluorescence generated by the fluorescent photons is negligible. Therefore only incident photons that are at wavelength λ_x are permitted to generate fluorescent photons.

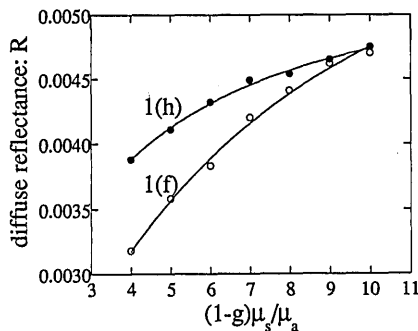


Fig. 2. Comparison of Eq. (2') with Monte Carlo calculations for two fiber geometries. The discrete points are Monte Carlo data, and the solid curves are the curve fits according to Eq. (2'). In 1(f), $k_0 = 0.0072$, $1/S' = 5.2$ and in 1(h), $k_0 = 0.0056$, $1/S' = 1.8$.

Initially we impose two temporary restrictions, which will be removed later: (1) The fluorescence anisotropy coefficient is equal to the tissue-scattering anisotropy coefficient g , and (2) the attenuation coefficients μ_t at the excitation and emission wavelengths are assumed to be equal. Since in the photon migration model the photon path is determined by g and μ_t , the incident excitation photon and the fluorescent photon induced by it will follow the exact same path in the above conditions. Figure 3 shows an example of a photon path in which an incident photon, entering with an initial weight of one, is scattered n times along its path and thus induces n fluorescent photons. When the notation $[w(\lambda_x)|w(\lambda_m)]$ represents the photon weights at the excitation and emission wavelengths, respectively, after the first scattering event a fluorescence photon is generated, and the photon weights are given by $[a(\lambda_x)|[1 - a(\lambda_x)]\phi(\lambda_x, \lambda_m)]$. After the second scattering event the weight of the incident photon is reduced again by the factor $a(\lambda_x)$, and the weight of the first fluorescent photon is reduced by the factor $a(\lambda_m)$. In the meantime a second fluorescence photon with weight $a(\lambda_x)[1 - a(\lambda_x)]\phi(\lambda_x, \lambda_m)$ is induced by the incident photon. Now by our notation the photon weights are written as $[a^2(\lambda_x)|[1 - a(\lambda_x)]\phi(\lambda_x, \lambda_m)a(\lambda_m) + a(\lambda_x)[1 - a(\lambda_x)]\phi(\lambda_x, \lambda_m)]$. When the photon emerges after n scattering events, the weights become

$$\left\{ a^n(\lambda_x) \left| \sum_{m=0}^{n-1} a^m(\lambda_x) [1 - a(\lambda_x)] \phi(\lambda_x, \lambda_m) a^{n-m-1}(\lambda_m) \right. \right\}.$$

Summing the total fluorescence weight over all the possible paths yields the bulk tissue fluorescence

$$\begin{aligned} F(\lambda_x, \lambda_m) &= \sum_{n=1}^{\infty} f_n(g) \left\{ \sum_{m=0}^{n-1} a^m(\lambda_x) [1 - a(\lambda_x)] \phi(\lambda_x, \lambda_m) a^{n-m-1}(\lambda_m) \right\} \\ &= [1 - a(\lambda_x)] \phi(\lambda_x, \lambda_m) \frac{R[a(\lambda_x), g] - R[a(\lambda_m), g]}{a(\lambda_x) - a(\lambda_m)}, \quad (3) \end{aligned}$$

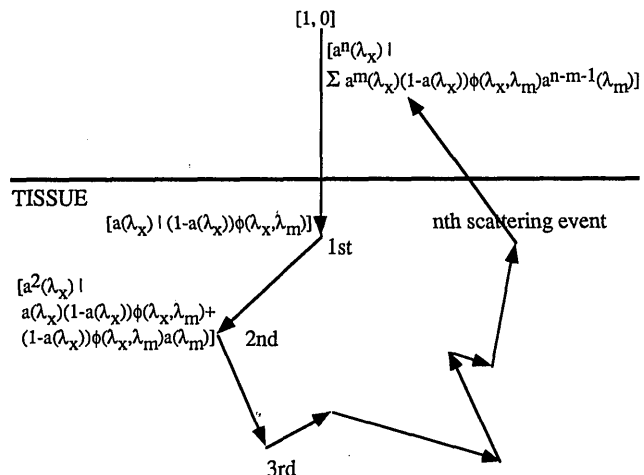


Fig. 3. Photon migration picture of fluorescence.

by making use of the relationship

$$R(a, g) = \sum_{n=1}^{\infty} a^n f_n(g).$$

Note that Eq. (3) is derived without any assumption about the experimental geometry or tissue boundary conditions, and the specific form of $f_n(g)$ is not utilized. This equation can thus be used to extract the system-independent quantum yield $\phi(\lambda_x, \lambda_m)$ for any experimental geometry as long as we measure F and R in the same manner. The algorithm propounded by Eq. (3) suggests that the intrinsic fluorescence extracted from measurement of the reflectance and fluorescence balances out any effects of geometry or boundary conditions.

To apply the model to realistic situations, we must now remove the two restrictions invoked in deriving Eq. (3). In our model g is assumed to be constant at all wavelengths of the fluorescence spectrum. This is based on the fact that the changes in g over wavelengths of interest are generally small¹¹ and do not significantly change the fluorescence spectrum. However, in the fluorescence event the photon is always emitted isotropically. We thus introduce an effective anisotropy coefficient g_{eff} defined as the average value of $(N - 1)$ forward directed scattering events with anisotropic coefficient g and a single isotropic fluorescence event with $g_{\text{fluorescence}} = 0$:

$$g_{\text{eff}} = \frac{(N - 1)g}{N}. \quad (4)$$

We chose N to be the peak position of the $f_n(g)$ curve rather than the mean number of scattering events, because the mean number is infinity, considering that $f_n(g)$ behaves as $n^{-3/2}$ when n approaches infinity. In the case of a semi-infinite slab of tissue, Monte Carlo simulations indicate that $N(1 - g) = 1.3$ for index-matched boundary conditions and 2.0 for index-mismatched boundary conditions (with relative indices of refraction of 1.4).¹²

Second, we initially assumed that μ_t , which determined the mean step length of photon migration, is the same at the excitation and emission wavelengths, so that the fluorescence photon follows the same path as the excitation photon. This is not necessarily true; thus the number of scattering events required for the fluorescence photon to emerge from the tissue will also change, and this must be taken into account to ensure that the final weight is correct. Consider the path of a fluorescence photon traversing the medium. On its way out the weight of this photon is reduced by a factor $w = [a(\lambda_m)]^{n_m}$, with n_m the number of steps taken by the fluorescence photon, whose step length is determined by $\mu_t(\lambda_m)$. We wish to express w in terms of n_x , the number of steps that would be taken if the photon step length were determined by $\mu_t(\lambda_x)$, compensating for the albedo accordingly. We introduce an effective albedo $a_{\text{eff}}(\lambda_m)$ defined so that $w = [a(\lambda_m)]^{n_m} = [a_{\text{eff}}(\lambda_m)]^{n_x}$, i.e., $a_{\text{eff}}(\lambda_m) = [a(\lambda_m)]^{n_m/n_x}$.

To obtain n_m/n_x , we consider a general result of random-walk theory,¹³ which states that the displacement D traveling in a random walk after n steps is related to the average value of its step length distribution l through the equation $D^2 = nl^2$. In our case the displacement is from the point in the tissue where the fluorescence photon is generated to the point on the surface where it emerges, and the step length is $1/\mu_t$. This displacement must be the same regardless of whether we use $1/\mu_t(\lambda_x)$ or $1/\mu_t(\lambda_m)$ as the average step length: $D^2 = n_x/\mu_t^2(\lambda_x) = n_m/\mu_t^2(\lambda_m)$. This gives

$$a_{\text{eff}} = a^{[\mu_t^2(\lambda_m)]/[\mu_t^2(\lambda_x)]} \quad (5)$$

for the index-matched boundary conditions.

In the index-mismatched boundary conditions, it is necessary to differentiate two types of fluorescence photon, those that are not internally reflected at the tissue surface and those that are internally reflected at least once and continue to travel within the tissue afterward. The effective albedo for the first type is the same as in the index-matched case. However, the effective albedo for the second type is assumed to be unchanged from the actual albedo $a(\lambda_m)$. According to the physical picture presented in Ref. 6, the weight change along a path between two points, both on the surface of an optically thick tissue sample, depends only on the albedo and g but not on the mean step length. Furthermore, it can be shown that the portion of the photon path after the first internal reflection event is on the average ~ 4 times longer than the portion before the first internal reflection event. Strictly speaking, $a_{\text{eff}}(\lambda_m)$ should be used to describe the change of weight before the first internal reflection and $a(\lambda_m)$ after that. Since the latter portion is dominant, we use $a(\lambda_m)$ for the entire path. Thus, more generally, the effective albedo can be approximated by

$$a_{\text{eff}} = r_d a + (1 - r_d) a^{[\mu_t^2(\lambda_m)]/[\mu_t^2(\lambda_x)]}, \quad (5')$$

where r_d is the probability of a photon being internally reflected at the boundary.¹⁴ In our case r_d is equal to 0 for the index-matched boundary conditions and 0.53 for the index-mismatched boundary conditions (with relative indices of refraction of 1.4).

When g and $a(\lambda_m)$ are replaced with g_{eff} and $a_{\text{eff}}(\lambda_m)$, and we note that $a_{\text{eff}}(\lambda_x)$ is just $a(\lambda_x)$, Eq. (3) becomes

$$F(\lambda_x, \lambda_m) = [1 - a(\lambda_x)]\phi(\lambda_x, \lambda_m) \times \frac{R[a(\lambda_x), g_{\text{eff}}] - R[a_{\text{eff}}(\lambda_m), g_{\text{eff}}]}{a(\lambda_x) - a_{\text{eff}}(\lambda_m)}. \quad (6)$$

Comparison with Monte Carlo simulations indicates that these two corrections improve the fits considerably. The error is typically reduced from more than 20% to $< 10\%$ (see below).

According to Eq. (6), when both diffuse reflectance and fluorescence are measured in the same manner and the appropriate corrections for g_{eff} and a_{eff} are

made, the effects of geometry and boundary conditions are canceled and the intrinsic fluorescence spectrum is extracted. In using Eq. (6) one should evaluate the albedo first from the reflectance by using the f_n curve for the given geometry and boundary condition.

Over a fairly wide range of tissue parameters, Eq. (6) can be further simplified by expressing the albedo a as a function of R . For the semi-infinite geometry and index-matched boundary conditions, Eq. (2) is used, with $-\ln(a)$ expanded as $(1 - a)$ since $\mu_s \gg \mu_a$. Then Eq. (6) becomes

$$F(\lambda_x, \lambda_m) = \phi(\lambda_x, \lambda_m) \{1 - R[a(\lambda_x), g_{\text{eff}}]\} R[a_{\text{eff}}(\lambda_m), g_{\text{eff}}], \quad (7)$$

which for single-wavelength excitation can be written clearly as

$$\phi(\lambda_m) = q \frac{F(\lambda_m)}{R[a_{\text{eff}}(\lambda_m), g_{\text{eff}}]}, \quad (8)$$

where $q = \{1 - R[a(\lambda_x), g_{\text{eff}}]\}$ is a proportionality constant that depends on the excitation wavelength. In Eq. (8) $F(\lambda_m)$ is measured in the experiment, whereas the effective reflectance, $R_{\text{eff}} = R[a_{\text{eff}}(\lambda_m), g_{\text{eff}}]$, cannot be directly measured. R_{eff} can be related to the measured diffuse reflectance, however, from Eqs. (2) and (5'):

$$\begin{aligned} \frac{\frac{1}{R_{\text{eff}}} - 1}{\frac{1}{R} - 1} &= \frac{1 - g}{1 - g_{\text{eff}}} \left[r_d + (1 - r_d) \frac{\mu_t^2(\lambda_m)}{\mu_t^2(\lambda_x)} \right] \\ &\approx \frac{1 - g}{1 - g_{\text{eff}}} \left[r_d + (1 - r_d) \frac{\mu_s^2(\lambda_m)}{\mu_s^2(\lambda_x)} \right]. \end{aligned} \quad (9)$$

Note that a and a_{eff} are both close to 1, and thus $\ln(a) = a - 1$. Since both g and μ_s vary little in different samples of the same tissue,¹⁵ Eq. (9) suggests that the shape of $\phi(\lambda_m)$ in Eq. (8) can be easily extracted by measuring F and R .

If we wish to extend this approach to other geome-

tries and boundary conditions, Eq. (7) must be modified by using Eq. (2'). However, as long as we interpret the measured diffuse reflectance as $R^{\text{obs}} = R/k_0$, Eq. (8) will remain the same, except for a different numerical proportionality constant $q = k_0[1 - R^{\text{obs}}[a(\lambda_x), g_{\text{eff}}]]$, depending on the specific geometry and boundary conditions through k_0 . Equation (9) also continues to hold if the measured diffuse reflectance is interpreted as R^{obs} . Thus, as long as F and R are measured in the same manner, the intrinsic line-shape information in $\phi(\lambda_m)$ can be extracted by using Eqs. (8) and (9). This is true because the fluorescence photons and the reflectance photons effectively follow the same path, so that all the system dependence of the fluorescence is retained in the diffuse reflectance measurement. The extracted $\phi(\lambda_m)$ is therefore a system-independent quantity, equivalent to measuring the fluorescence from a thin tissue specimen that is unaffected by absorption and scattering. Furthermore, in certain practical situations in which the geometry and boundary conditions can be made reproducible,¹ the constant q can be calibrated, and the measurement will then yield calibrated intensity information as well.

3. Comparison of Analytical Expressions with Simulations and Experiments

A. Monte Carlo Simulations for a Semi-infinite Slab

Both Monte Carlo simulations and tissue experiments have been carried out to verify the theory presented above. In the Monte Carlo calculations the tissue optical parameters, μ_a , μ_s , g , and ϕ , of human aorta intima and media,¹⁵ summarized in Table 2, were utilized to simulate the fluorescence. The results were compared with our model, Eq. (6), as well as with both the Eddington approximation and the δ -Eddington approximation to diffusion theory discussed above.^{16,17} In each simulation 10,000 incident photons in a 1-mm plane wave impinged perpendicularly upon a 10-mm-thick slab of tissue, and the number of all the fluorescence photons emerging from the upper surface was recorded. No photons were observed to emerge from the back surface.

In Fig. 4 the results of Monte Carlo simulations are

Table 2. Summary of the Aortic Tissue Optical Parameters from the Literature¹⁵ Utilized in the Monte Carlo Simulations

Intima									
$\lambda(\text{nm})$	476 ^a	500	520	540	560	580	600	620	640
$\phi(\text{au})$		66	100	95	83	61	49	34	24
$\mu_a(\text{mm}^{-1})$	1.3	1.0	0.8	1.0	0.8	1.0	0.4	0.4	0.4
$\mu_s(\text{mm}^{-1})$	29.0	27.5	24.8	24.7	23.3	21.8	20.4	20.0	19.6
g	0.84	0.84	0.84	0.84	0.84	0.84	0.84	0.84	0.84
Media									
$\lambda(\text{nm})$	476 ^a	500	520	540	560	580	600	620	640
$\phi(\text{au})$		66	100	95	83	61	49	34	24
$\mu_a(\text{mm}^{-1})$	0.70	0.55	0.50	0.60	0.45	0.50	0.25	0.24	0.25
$\mu_s(\text{mm}^{-1})$	48.0	45.5	43.5	40.5	38.5	37.0	36.0	35.0	33.5
g	0.9	0.9	0.9	0.9	0.9	0.9	0.9	0.9	0.9

^aExcitation wavelength.

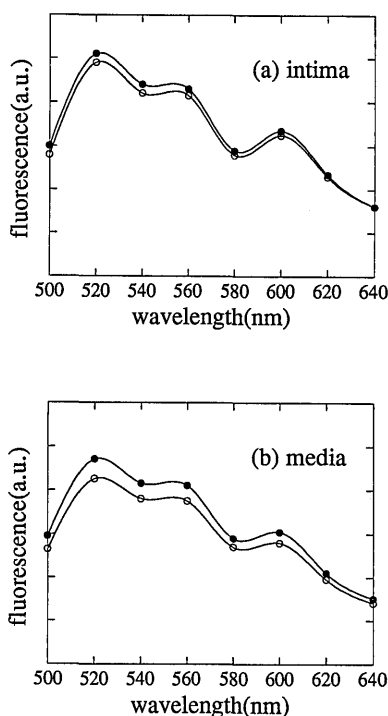


Fig. 4. Comparison of photon migration model with Monte Carlo for (a) intima and (b) media. The open circles are data points from Eq. (6), and the solid circles and Monte Carlo simulations. The curves are cubic spline curve fits to the data points.

compared with Eq. (6) for two cases using tissue parameters from arterial intima and media,¹⁵ with a semi-infinite geometry and an index-matched boundary condition assumed. The data points are connected by cubic spline curve fits, reflecting the nature of tissue fluorescence spectra, which are observed to be smooth. The model always predicts a slightly lower fluorescence than does the Monte Carlo calculations. When the known tissue parameters from intima are utilized [Fig. 4(a)], the difference between the model and Monte Carlo simulation is $< 5\%$ over the entire spectrum. In this case the anisotropy coefficient is 0.84. When g is raised to 0.9, as is measured for aortic media, the difference between the Monte Carlo simulation and Eq. (6) is of the order of 10% [Fig. 4(b)]. The reason for the discrepancy at higher values of g can be understood from our evaluation of g_{eff} in Eq. (4). Since N approaches infinity as g approaches one, g_{eff} approaches g at higher g values. In the limit that g approaches one the diffuse reflectance goes to zero; thus the model, Eq. (6), predicts zero fluorescence intensity, which is clearly incorrect. On the other hand, g_{eff} is exactly the same as g when photons are scattered isotropically. Thus the approximation for g_{eff} works better for lower values of g . Nevertheless the comparison with the Monte Carlo calculations shows that the model yields good results, especially in the fluorescence line shape, which should permit the use of simple algorithms based on measurements of fluorescence and reflectance. Similar results are also obtained for index-mismatched boundary conditions.¹²

Figure 5 shows the comparison of the Monte Carlo simulations with the Eddington and δ -Eddington approximations of diffusion theory.^{14,15} The δ -Eddington approximation provides the best overall fit to the simulations, because it deals with the highly anisotropic scattering events and the isotropic fluorescence events separately and accurately. However, as stated earlier, neither of these approximations can provide a simple algorithm for extracting the intrinsic fluorescence of the tissue, as would be required for development of a diagnostic method based on the biochemical or morphological tissue properties.

B. Fluorescence/Reflectance Experiments

To test Eq. (8) experimentally, fluorescence and diffuse reflectance spectra from human aortic media were collected by a Spex spectrofluorimeter. This instrument focuses the beam to a 2-mm spot on the tissue and collects the fluorescence light in a small solid angle at 23° with respect to the tissue surface normal direction. The tissue specimens were collected at autopsy within 24 h of death. On receipt samples were snap frozen in liquid nitrogen/isopentane and stored at -70°C until the experiments. At the time of the experiments specimens were passively thawed to room temperature and were kept moist in a buffered isotonic saline solution. The intimal layer was removed before spectra were obtained.

Tissue samples were placed in a quartz cuvette with saline, and the human side was oriented toward the window to be irradiated. The quartz material is

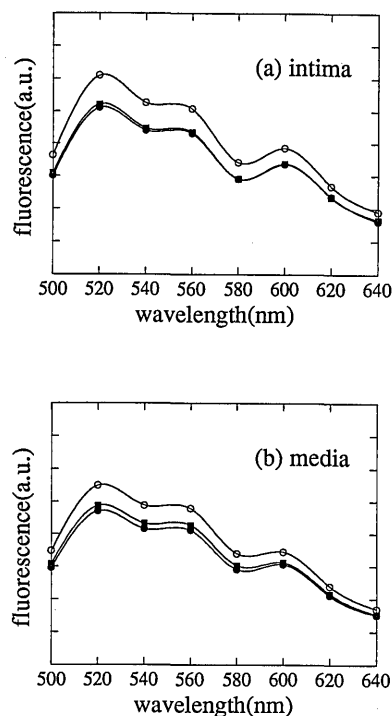


Fig. 5. Comparison of diffusion theory models with Monte Carlo for (a) intima and (b) media. The solid circles are from Monte Carlo simulations, the open circles and solid squares are from diffusion theory, Eddington approximation, and δ -Eddington approximation, respectively. The curves are cubic spline curve fits.

assumed to be index matched with the tissue, and then the tissue-quartz-air boundary is simplified as a tissue-air boundary with the relative refractive indices of 1.4. Fluorescence, $F(\lambda_m)$ in Eq. (8), was obtained with 476-nm excitation, and emission was measured from 500 to 650 nm in 2-nm intervals. Diffuse reflectance $R[a(\lambda), g]$ was measured from 450 to 650 nm in 2-nm intervals. Reflectance from a cuvette of BaSO₄ powder was also measured and used as the reflectance standard. Both the fluorescence and the reflectance experiments were carried out in the exactly identical geometry. $R[a(\lambda), g]$ was changed to $R[a_{\text{eff}}(\lambda_m), g_{\text{eff}}]$ by using Eq. (9) and aorta tissue parameters, g and μ_s , from the literature.¹⁵ To test the effect on the model of changing the absorption coefficient, we soaked aortic media for various times in diluted lysed whole blood. The resulting fluorescence spectra showed the effect of reabsorption of the fluorescence light from the oxyhemoglobin, as is discussed below. After the fluorescence and reflectance spectra were obtained, the specimens were frozen again in liquid nitrogen and mounted on microtome chucks. 10- μm -thick sections were cut, placed on glass slides, and covered with a drop of saline and by glass cover slips to keep the tissue slices moist. The intrinsic fluorescence line shape $\phi(\lambda_m)$ was measured from the 10- μm sections for comparison with that obtained from the model described by Eq. (8). The spectral resolution in all the fluorescence measurements is 4 nm full wave at half-maximum. Usually several scans were taken from each sample, and the spectra were observed to be reproducible. The data presented below are single-scan spectra; no average was taken.

In Fig. 6(a) the fluorescence and diffuse reflectance spectra observed from optically thick aortic media soaked in saline and the intrinsic fluorescence spectrum measured from a 10- μm section of that piece of media are compared. The bulk tissue fluorescence spectra show the typical line shape expected from the elastinrich media,¹ and the reflectance matches previously reported data.¹⁵ When the fluorescence spectrum is divided by the effective reflectance spectrum according to Eq. (8), the curve maximum shifts to a slightly shorter wavelength, as shown in Fig. 6(b). Also shown in Fig. 6(b) is the intrinsic fluorescence spectrum. Both spectra are normalized to the same integrated intensity for comparison; the match is remarkable, as can be seen from the calculated residuals also shown in this figure.

In Fig. 7(a) the fluorescence and diffuse reflectance spectra obtained from optically thick aortic media, which had been soaked overnight in diluted lysed whole blood, are compared. The two valleys in the fluorescence spectrum at 540 and 575 nm are due to absorption of the emission light by the oxyhemoglobin.¹ The resulting fluorescence spectrum is heavily distorted from the intrinsic fluorescence of the system. However, the effect of the hemoglobin is removed from the spectrum by using the algorithm of Eq. (8),

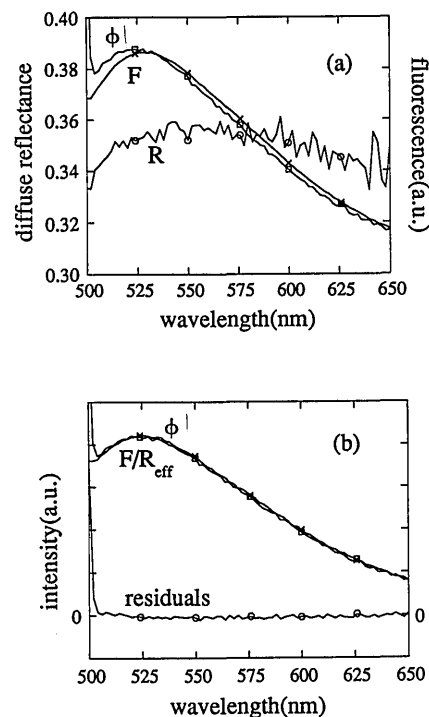


Fig. 6. Experimental data from human aortic media soaked in saline. (a) Comparison of optically thick fluorescence (crosses), reflectance spectrum (circles), and thin fluorescence (squares). (b) Comparison of the intrinsic fluorescence extracted by using the model (crosses) and measured from thin sample (squares); residuals (circles) are included.

as shown in Fig. 7(b). Here the fluorescence from a 10- μm section of that piece of media again matches very well with that calculated from Eq. (8). The algorithm has effectively removed the distortion, caused by absorption, scattering, geometry, and boundary conditions from the observed signal of the bulk tissue spectrum, allowing the intrinsic fluorescence spectrum to be extracted.

4. Discussion and Applications

The result of the photon migration approach to tissue fluorescence is that by measuring the reflectance spectrum over the same wavelength range and in the same geometrical configuration as the fluorescence spectrum, an intrinsic fluorescence line shape can be extracted that is undistorted by the scattering and absorption in the tissue. Thus the distortion of the fluorescence line shape associated with the absorption of the excitation and emission light, tissue boundary conditions, and geometry of irradiation and collection can be removed. This provides a connection between *in vitro* microspectroscopy experiments on thin tissue sections and *in vivo* clinical data, despite the fact that these two types of experiment are performed in different geometries. Since ultimately microspectroscopy provides the fluorescence line shapes of the individual morphological structures $\phi(\lambda_m)$, one can deconvolve the contribution of each of the morphological structures, using the simple relation

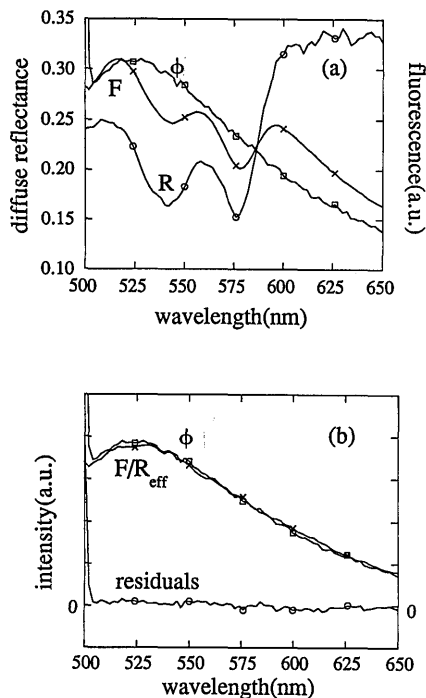


Fig. 7. Experimental data from human aortic media soaked in lysed blood. (a) Comparison of optically thick fluorescence (crosses), reflectance spectrum (circles), and thin fluorescence (squares). (b) Comparison of the intrinsic fluorescence extracted by using the model (crosses) and measured from thin sample (squares); residuals (circles) are included.

$$\phi(\lambda_m) = \sum_i c_i' \frac{(\mu_a)_i}{\mu_a} \phi_i(\lambda_m) = \sum_i c_i \phi_i(\lambda_m), \quad (10)$$

where c_i is proportional to the individual chromophore concentration and can be obtained by fitting the experimental data to Eq. (10).

As discussed above, Eq. (8) is valid over a range where $\mu_s(1 - g)/\mu_2$ is < 10 , i.e., the range over which Eq. (2) is valid. In addition, since we expanded $\ln(a)$ to $a - 1$ to obtain Eq. (7), Eq. (8) becomes invalid for large values of μ_a , say $\mu_a > 10\% \mu_s$. This yields the range of validity for Eq. (8) to be $10 < \mu_s/\mu_a < 100$ for human aortic media ($g = 0.9$). Outside this range the albedo should be evaluated first from the reflectance by using the f_n curve in the given geometry and boundary conditions, and then Eq. (6) should be utilized instead of Eq. (8). Moreover the photon migration model is derived in the condition that the tissue fluorophores and absorbers are assumed to be homogeneously distributed. The situation can be quite different when the tissue consists of several layers in which the optical parameters are disparate. We are currently exploring the possibility of expanding this methodology to handling multilayered tissues.

The method for extracting intrinsic fluorescence presented in this paper is related to an earlier developed method,¹ in which the bulk fluorescence $F(\lambda_m)$ is given by

$$F(\lambda_m) = k\mu_a\phi(\lambda_m)/A(\lambda_x, \lambda_m), \quad (11)$$

with μ_a and ϕ as defined above, k a constant determined by the geometry and relative refractive indices, and A an attenuation line shape that incorporates the net effect of absorption and scattering. Equation (11) provides the basis for a curve-fitting algorithm in which the intrinsic fluorescence can be extracted from F in an experimental arrangement in which the light delivery and collection are fixed. This algorithm was applied to the diagnosis of artery wall tissue.¹ A fiber-optic catheter probe with fixed delivery and collection geometry was employed. The line shapes for ϕ and A were expressed as linear combinations of spectral components corresponding to constituent tissue chromophores. With Eq. (11) the attenuation A was then evaluated by measuring fluorescence from both optically thick and thin samples of known composition. The observed fluorescence line shape F from an unknown artery samples could then be fit to Eq. (11), and an accurate tissue diagnosis could be made from the resulting fit coefficients. The details are given in Ref. 1.

The procedure for extracting intrinsic fluorescence is consistent with that of Eq. (8), provided that A is identified with μ_a/R_{eff} . The success of the curve-fitting approach of Eq. (11) in extracting ϕ can thus be considered as additional support for the validity of Eq. (8). Equation (8) is more generally applicable, because it also provides a method of extracting the intrinsic fluorescence directly from the experimental determination of F and R , even in situations in which the geometry is not fixed and/or knowledge of the attenuation is incomplete. However, the curve-fitting procedure provides an alternative method for extracting ϕ in cases where the diffuse reflectance information is not conveniently obtained.

Perhaps the most important feature of the algorithm resulting from the photon migration model of tissue fluorescence is that it can be readily applied in a clinical setting. All clinical apparatuses that are used to measure fluorescence can be easily modified for the determination of the diffuse reflectance. Only a common white-light source and a beam splitter need to be added to the light delivering subsystem to determine the reflectance. However, one must avoid the specular reflectance that may return through a fiber-optic probe, or careful subtraction of the specular component must be carried out.

In addition to its application to human tissue fluorescence, the methodology presented here has broader applications. Studies of fluorescence in other turbid situations, such as binding to large polymers of DNA or whole cells, would benefit from measuring the reflectance and applying the algorithm described by Eq. (8). Similarly this approach can be used to model the Raman-scattering spectroscopy from human tissues or other turbid situations.¹⁸ In this case the product of the Raman cross section times the density, $\rho\sigma_{\text{Raman}}/\mu_t(\lambda_x)$, replaces the term $[1 - a(\lambda_x)]\phi(\lambda_x, \lambda_m)$ in Eq. (3).

5. Conclusions

In this paper we have presented a model of fluorescence from human tissue based on the photon migration theory, which can be used to extract the intrinsic fluorescence spectrum from the optically thick tissue fluorescence spectrum even when the latter has been distorted by the interplay of tissue scattering, absorption, refractive index, excitation, and collection geometry. The validity of the model has been verified by Monte Carlo simulations and laboratory experiments. We demonstrated that by measuring the diffuse reflectance spectrum over the same wavelength range as the fluorescence spectrum, the intrinsic tissue fluorescence spectrum can be easily obtained to provide useful information of the tissue fluorophores. The simplicity of this approach, both in the experiment apparatus required to obtain the necessary data, and the relationship of the resulting spectra to the intrinsic tissue fluorescence, makes it a promising methodology for clinical implementation.

Appendix A: One-Dimensional Diffusion Calculation for Fluorescence

For a semi-infinite, one-dimensional slab the tissue fluorescence can be calculated within diffusion theory by using the Eddington approximation.¹⁶ The problem can be broken into two parts: (1) determination of the incident light distribution within tissue excited by a plane wave incident on a slab and (2) determination of the diffusion from a point source within the tissue. Both of these problems have been examined in detail by Ishimaru¹⁶ and will be reviewed only briefly here.

For a plane wave of flux density $F_0(\text{mW mm}^{-2} \text{Hz}^{-1})$ incident on a slab of tissue, the specific intensity at a depth z in the tissue, $I(z, \omega)(\text{mW mm}^{-2} \text{sr}^{-1} \text{Hz}^{-1})$, can be divided into two parts, the reduced incident intensity $I_{ri}(z, \omega)$ and the diffuse intensity I_d . $I_{ri}(z, \omega)$ is given by

$$I_{ri}(z, \omega) = F_0 \exp(-\mu_t z) \delta(\omega - \omega_z), \quad (\text{A1})$$

where $\mu_t(\text{mm}^{-1})$ is the total attenuation coefficient given by the sum of the scattering coefficient μ_s and the absorption coefficient μ_a , and $\delta(\omega - \omega_z)(\text{sr}^{-1})$ is the solid-angle δ -function. The diffuse intensity component is obtained by solving the diffusion equation which for this case is

$$\frac{d^2 U_d(z)}{dz^2} - \kappa_d^2 U_d(z) = Q_0 \exp(-\mu_t z). \quad (\text{A2})$$

In Eq. (A2) the average diffuse intensity,

$$U_d(z)(\text{mW mm}^{-2} \text{Hz}^{-1}) = \frac{1}{4\pi} \int_{4\pi} I_d d\omega (\text{mW mm}^{-2} \text{Hz}^{-1}),$$

$$Q_0 = \frac{3F_0(\mu_s \mu_{tr} + g \mu_s \mu_t)}{4\pi},$$

$$\kappa_d = (3\mu_{tr} \mu_a)^{1/2}.$$

The anisotropy coefficient g describes the angular

dependence of the scattering and $\mu_{tr} = \mu_s(1 - g) + \mu_a$. In index-matched boundary conditions

$$U_d(z) - h \frac{dU_d(z)}{dz} + \frac{Q_1}{2\pi} = 0 \text{ at } z = 0,$$

$$U_d(z) = 0 \text{ at } z = +\infty, \quad (\text{A3})$$

where $h = 2/(3\mu_{tr})$ and $Q_1 = [(\mu_s g)/\mu_{tr}]F_0$, the solution for $U_d(z)$ is

$$U_d(z) = A \exp(-\mu_t z) + C_2 \exp(-\kappa_d z), \quad (\text{A4})$$

where

$$A = \frac{Q_0}{(\mu_t^2 - \kappa_d^2)},$$

$$C_2 = \frac{-A(1 + \mu_t h)}{(1 + \kappa_d h)} - \frac{Q_1}{2\pi(1 + \kappa_d h)}.$$

Thus the total intensity at depth z is given by

$$I_{\text{total}}(z) = 4\pi U_d(z) + I_{ri}(z). \quad (\text{A5})$$

Now that the intensity of the incident light at depth z within the tissue is known, we need to determine the fluorescence intensity that returns upward back to the tissue surface for detection. In this problem we are considering diffusion from a uniform layer of point (fluorescence) sources within the tissue. The position of the source layer is considered to be at $z = 0$, with the z axis increasing upward toward the tissue surface, where $z = z_0$. The diffusion equation for this situation is

$$\frac{d^2 U_d(z)}{dz^2} - \kappa_d^2 U_d(z) = \frac{-3}{4\pi} \mu_{tr} P_0 \delta(z = 0), \quad (\text{A6})$$

with the boundary conditions

$$U_d(z) + h \frac{dU_d(z)}{dz} = 0 \text{ at } z = z_0,$$

$$U_d(z) = 0 \text{ at } z = -\infty. \quad (\text{A7})$$

The solution is found to be

$$U_d(z) = B \exp(\kappa_d z) + \frac{3P_0}{8\pi} \frac{\mu_{tr}}{\kappa_d} \exp(-\kappa_d z),$$

$$0 < z < z_0, \quad (\text{A8})$$

where

$$B = \frac{P_0}{4\pi} \exp(-2\kappa_d z_0) \frac{1 - 3\mu_{tr}/2\kappa_d}{1 + 2\kappa_d/3\mu_{tr}}.$$

The total flux emitted at the surface ($z = z_0$) can be calculated from

$$F_d = \frac{-4\pi}{3\mu_{tr}} \frac{dU_d(z)}{dz} = CP_0 \exp(-\kappa_d z_0), \quad (\text{A9})$$

with $C = 3\mu_{tr}/(3\mu_{tr} + 2\kappa_d)$.

The observed fluorescence can now be calculated as

$$\begin{aligned}
 & F(\lambda_x, \lambda_m) \\
 &= \int_0^{+\infty} dz \{ [4\pi A(\lambda_x) + F_0] \\
 &\quad \times \exp[-\mu_t(\lambda_x)z] + 4\pi C_2(\lambda_x) \exp[-\kappa_d(\lambda_x)z] \} \\
 &\quad \times \mu_a(\lambda_x) \phi(\lambda_x, \lambda_m) C(\lambda_m) \exp[-\kappa_d(\lambda_m)z] \\
 &= \mu_a(\lambda_x) \phi(\lambda_x, \lambda_m) \\
 &\quad \times \left[\frac{4\pi A(\lambda_x) + F_0}{\mu_t(\lambda_x) + \kappa_d(\lambda_m)} + \frac{4\pi C_2(\lambda_x)}{\kappa_d(\lambda_x) + \kappa_d(\lambda_m)} \right] C(\lambda_m),
 \end{aligned}
 \tag{A10}$$

where λ_x and λ_m are the excitation and emission wavelengths, respectively. The solution of the δ -Eddington approximation¹⁷ is also given by Eq. (A10) with μ_a , μ_s , and g replaced by $\mu_a' = \mu_a$, $\mu_s' = (1 - g^2)\mu_s$, $g' = g/(1 + g)$.

Support from National Institutes of Health (NIH) R01-CA53717 is gratefully acknowledged. This study was completed at the NIH-supported Massachusetts Institute of Technology Laser Biomedical Research Center (NIH RR02594). The authors thank Firooz Partovi for valuable contributions and discussions.

References

1. R. Richards-Kortum, R. P. Rava, M. Fitzmaurice, L. L. Tong, N. B. Ratliff, J. R. Kramer, and M. S. Feld, "A one-layer model of laser-induced fluorescence for diagnosis of disease in human tissue: applications to atherosclerosis," *IEEE Trans. Biomed. Eng.* **36**, 1222-1232 (1989).
2. L. I. Deckelbaum, J. K. Lam, H. S. Cabin, K. S. Clubb, and M. B. Long, "Discrimination of normal and atherosclerotic aorta by laser induced fluorescence," *Lasers Surg. Med.* **7**, 330-335 (1987).
3. M. Sartori, R. Sauerbrey, S. Kubodera, F. Tittel, R. Robert, and P. Henry, "Autofluorescence maps of atherosclerotic human arteries—a new technique in medical imaging," *IEEE J. Quantum Electron.* **23**, 1794-1797 (1987).
4. R. R. Alfano, G. C. Pradhan, G. C. Tang, B. B. Das, and K. M. Yoo, "Optical spectroscopy may offer novel diagnostic approaches for the medical profession," in *Laser Non-Surgical Medicine: New Challenges for an Old Application*, L. Goldman, ed. (Technomic, Lancaster, Pa., 1991), and references therein.
5. R. Nossal, R. F. Bonner, and G. H. Weiss, "Influence of path length on remote optical sensing of properties of biological tissue," *Appl. Opt.* **28**, 2238-2244 (1989).
6. J. Wu, F. Partovi, M. S. Feld, and R. P. Rava, "Diffuse reflectance from turbid media: an analytical model of photon migration," *Appl. Opt.* **32**, 1115-1121 (1993).
7. S. A. Prahl, M. Keijzer, S. L. Jacques, and A. J. Welch, "A Monte Carlo model of light propagation in tissue," in *Dosimetry of Laser Radiation in Medicine and Biology*, G. Miller, D. Sliney, and R. Potter, eds. Proc. Soc. Photo-Opt. Instrum. Eng. **IS5**, 102-111 (1989).
8. S. L. Jacques, C. A. Alter, and S. A. Prahl, "Angular dependence of HeNe laser light scattering by human dermis," *Lasers Life Sci.* **1**, 309-333 (1987).
9. J. D. Jackson, *Classical Electrodynamics* (Wiley, New York, 1975).
10. S. A. Prahl, "Light transport in tissue," Ph.D. dissertation (University of Texas at Austin, Austin, Tex., 1988).
11. W. Cheong, S. A. Prahl, and A. J. Welch, "A review of the optical properties of biological tissues," *IEEE J. Quantum Electron.* **26**, 2166-2185 (1990).
12. J. Wu, "Light-tissue interactions: applications to diffuse reflectance and fluorescence spectroscopy of human tissue," M.S. thesis (Department of Physics, Massachusetts Institute of Technology, Cambridge, Mass., 1992).
13. S. K. Ma, *Statistical Mechanics* (World Scientific, Philadelphia, Pa., 1985).
14. W. G. Egan and T. W. Hilgeman, *Optical Properties of Inhomogeneous Materials* (Academic, New York, 1979).
15. M. Keijzer, R. R. Richards-Kortum, S. L. Jacques, and M. S. Feld, "Fluorescence spectroscopy of turbid media: autofluorescence of human aorta," *Appl. Opt.* **28**, 4286-4292 (1989).
16. A. Ishimaru, *Wave Propagation and Scattering in Random Media* (Academic, Orlando, Fla., 1978), Vol. 1.
17. J. H. Joseph, W. J. Wiscombe, and J. A. Weinman, "The delta-Eddington approximation for radiative transfer," *J. Atmos. Sci.* **33**, 2452-2459 (1976).
18. R. P. Rava, J. J. Baraga, and M. S. Feld, "Near infrared Fourier transform Raman spectroscopy of human artery," *Spectrochim. Acta A* **47**, 509-512 (1991).